MATERIALS CHEMISTRY
FRONTIERS

CHINESE CHEMICAL SOCIETY

ROYAL SOCIETY OF CHEMISTRY

RESEARCH ARTICLE

View Article Online
View Journal

Cite this: DOI: 10.1039/d5qm00916b

# Cu,S,N heteroatom-tailored carbon quantum dots enabling efficient electrochemical $CO_2$ reduction to acetate and formate

Suanto Syahputra,[a] Florence Vacandio,[a] Véronique Wernert,[a] Emanuela Sgreccia,[b] Saulius Kaciulis,[c] Maria Luisa Di Vona *[b] and Philippe Knauth *[a]

Received 22nd December 2025,
Accepted 1st March 2026

DOI: 10.1039/d5qm00916b

rsc.li/frontiers-materials

Electrochemical $CO_2$ reduction (ECO2R) offers a promising route to mitigate $CO_2$ emissions while generating value-added chemicals. Here, we report the synthesis of heteroatom-modified carbon quantum dots (CQDs) *via* a green hydrothermal method using citric acid, glucosamine, urea, and cysteine as precursors, with copper incorporation. Structural characterization by XPS and Raman spectroscopy confirmed successful Cu, S, and N doping, while water contact angle measurements revealed precursor-dependent surface hydrophilicity. Electrodes prepared with 80 wt% CQDs and 20 wt% anion-exchange ionomer exhibited high electrochemically active surface areas. Among the series, Cu,S,N-CQD-GAH derived from glucosamine, showing lower hydrophilicity, delivered the most effective ECO2R performance. This catalyst selectively produced formate and acetate, as verified by HPLC and $^1$H NMR, achieving acetate formation rates up to 1.5 mmol $g_{cat}^{-1}$ $h^{-1}$ at −0.4 V *vs.* RHE. The half-cell energy efficiency peaked at 52.3% with a faradaic efficiency of 66.8% at −0.2 V *vs.* RHE. The enhanced activity is attributed to nitrogen functionalities in aminic/pyridinium oxide forms and the presence of Cu(I), which promotes C–C coupling. In contrast, sulfur-free or Cu(II)-rich CQDs exhibited diminished activity. Long-term chronoamperometry confirmed stable current densities after an initial activation period, highlighting the durability of the Cu,S,N-CQD catalysts.

## 1. Introduction

Electrochemical $CO_2$ reduction (ECO2R) allows the conversion of carbon dioxide, a main greenhouse gas, into high-value chemicals or fuels ideally by renewable electricity, contributing to carbon footprint mitigation and closing the carbon cycle.[1–3] Despite its potential, ECO2R remains kinetically challenging due to the high dissociation energy of the C=O bond ($\approx$800 kJ $mol^{-1}$ (ref. 4)) and the numerous electron transfer and protonation steps involved;[5] consequently, a high overpotential is generally required for carbon dioxide reduction and multiple complex reaction pathways are possible. Furthermore, the hydrogen evolution reaction (HER), which occurs in the same potential range, is a potent competitor, kinetically favoured over the ECO2R in aqueous electrolytes especially in acidic conditions, so that neutral or mildly alkaline media and appropriate electrocatalysts, unfavourable for the HER, must be applied.[5] Diluted $HCO_3^-$ solutions with a near neutral pH have been identified as optimal electrolytes for the ECO2R,[6] because $CO_2$ reacts to carbonate in strongly alkaline solutions and the HER is favoured in concentrated $HCO_3^-$.[1,6]

$CO_2$ can be electrochemically reduced to several products, depending on the conditions, electrode materials, and catalysts used. The development of efficient, selective, and stable catalysts is one of the major challenges of the ECO2R.[3,7–9] The product distribution depends not only on the electrocatalyst and support but also on reaction conditions including temperature, electrolyte composition, and pH. Selective catalysts are highly desirable, as they minimize downstream separation and purification steps, improving economic feasibility.[10]

Various metals can catalyse the ECO2R, but some of them are quite toxic and others rare or expensive. The formation of formate can be catalysed for example by Hg, Bi, Pb, Sn and In; Pt, Ni, Fe and Ti catalyse preferentially the HER.[6] Beyond $C_1$ products such as formate, optimized catalysts can generate multi-carbon ($C_{2+}$) products providing a means for the production of other valuable chemicals. However, the formation of $C_{2+}$ products (such as acetate) by the ECO2R is a particularly

---

[a] *Aix Marseille Univ, CNRS, MADIREL (UMR 7246) and International Laboratory: Ionomer Materials for Energy (LIME), Campus St Jérôme, 13013 Marseille, France. E-mail: suanto.syahputra@univ-amu.fr, florence.vacandio@univ-amu.fr, veronique.wernert@univ-amu.fr*

[b] *Tor Vergata University of Rome, Dep. Industrial Engineering and International Laboratory: Ionomer Materials for Energy (LIME), 00133 Roma, Italy. E-mail: emanuela.sgreccia@uniroma2.it*

[c] *Institute for the Study of Nanostructured Materials, ISMN-CNR, 00015 Monterotondo Stazione, Roma, Italy. E-mail: saulius.kaciulis@cnr.it*

challenging endeavour.[1] Among the non-rare, non-toxic metals, copper and copper compounds are today the only well-known catalysts for producing various multi-carbon products,[1,2,6,11–15] but they suffer from a low product selectivity[1,6] and their stability needs improvement.

Carbon-based catalysts, on the other hand, are attractive for their low cost, tunability, and benign nature. Nitrogen is the most studied heteroatom in carbon materials: it has a larger electronegativity than carbon leading to the formation of local dipoles that can enhance $CO_2$ adsorption.[6,16] Nitrogen-doped carbon materials, including nanodiamond and carbon blacks co-doped with metals, have shown high faradaic efficiencies (FE) for formate[5,16,17] and even acetate formation through pathways involving oxalate or Fe–N coordination.[17–19]

Carbon quantum dots (CQDs) have attracted considerable interest for their applications in photocatalytic and electrocatalytic $CO_2$ reduction[20] as well as in the oxygen reduction reaction (ORR).[21–23] Due to their high surface area and abundance of low-coordination active sites (*e.g.*, edges, defects, and basal planes), nanodots exhibit enhanced catalytic performance.[6] CQDs can be tailored *via* various routes, allowing precise control over dopant concentration and the spatial distribution of functional groups.[24] According to our experience, hydrothermal synthesis is a particularly attractive method, because it allows to tailor efficiently the content and position of many heteroatoms, including N, S, B.[22] The precursor choice strongly influences CQD properties: citric acid generally yields hydrophilic CQDs rich in pyrrolic, aminic, or pyridinic nitrogen, whereas glucosamine tends to form more hydrophobic CQDs with nitrogen mainly in graphitic configurations.[24] Nitrogen-doped CQD were already tested for the ORR[21] where it was shown that graphitic nitrogen had a higher electrocatalytic activity for the ORR than in pyrrolic and pyridinic positions.[23] This enhanced performance is attributed to the formation of local dipoles between electronegative nitrogen atoms and neighbouring electropositive carbon atoms, which promotes the "bridge side-on" adsorption of $O_2$ molecules, an effect that also favours $CO_2$ adsorption.[4,9] Heteroatom co-doping by sulfur can further improve the electrocatalytic properties of CQDs by modulating their electronic structure and stabilizing key intermediates.[22] In contrast, undoped $sp^2$-conjugated carbon materials, composed solely of neutral carbon atoms, exhibit limited interaction with $CO_2$ molecules.[6]

Building on this literature and recognizing the catalytic advantages of heteroatom-doped CQDs and copper-based nanostructures, particularly for $C_{2+}$ product formation, we developed a series of electrocatalysts based on Cu, N, and S co-doped CQDs synthesized *via* the hydrothermal route. The incorporation of a highly efficient hydroxide-conducting ionomer as an electrode binder significantly improves the catalytic activity in alkaline media, by promoting $OH^-$ ion transport to and from the active sites within the catalyst layer.[1,25] This ionomer, poly(2,6-dimethylphenylene oxide) functionalized with trimethylammonium groups on long (pentyl) side chains (PPO-LC, chemical formula in the SI, Fig. S1), was previously shown to boost the ORR performance.[1,25,26] However, since ionomers are not electronically conductive, they may insulate a fraction of catalytic particles.[8] An optimal ionomer content of 20 wt% balances ionic conductivity and particle accessibility.[8,25]

In this work, we report the synthesis, characterization, and electrocatalytic performance of Cu,S,N and Cu,N co-doped CQDs combined with PPO-LC ionomer. Particular attention is given to their activity, selectivity, and stability for ECO2R.

## 2. Materials and methods

### 2.1. Synthesis

All chemical products were obtained from Sigma-Aldrich (Milano, Italy) and were used as received. Carbon paper (AvCarb EP55) was purchased from the Fuel Cell Store.

**2.1.1. Cu,S,N-doped CQD from citric acid (Cu,S,N-CA).** In a typical procedure, 1.5 mmol of citric acid (CA, 0.29 g), 0.3 mmol of urea (0.02 g), 1.0 mmol of L-cysteine (0.12 g), and 0.17 mmol of copper(II) acetate ($Cu(OAc)_2$, 0.03 g) were dissolved in 7 mL of deionized water under stirring. The resulting solution was transferred into a Teflon-lined stainless-steel autoclave and subjected to hydrothermal treatment at 200 °C for 10 h using a heating rate of 5 °C $min^{-1}$. After cooling to room temperature, the mixture was centrifuged at 6000 rpm for 20 min to separate the solid and liquid phases. Both fractions were examined under UV light (365 nm), confirming that the solid fraction contained the luminescent CQDs. The CQDs were washed twice with deionized water, followed by dialysis for 48 h (MWCO = 1 kDa) to remove residual impurities. Finally, the purified CQDs were dried under reduced pressure using a rotary evaporator at 50 °C.

**2.1.2. Cu,S,N-doped CQD from glucosamine (Cu,S,N-GAH).** For the synthesis of Cu,S,N-GAH, 2.1 mmol of glucosamine hydrochloride (GAH, 0.45 g), 1.5 mmol of L-cysteine (0.18 g), and 0.17 mmol of copper(II) acetate ($Cu(OAc)_2$, 0.03 g) were used as precursors. The reagents were dissolved in 3 mL of deionized water under stirring, followed by the addition of 2 mL of *N*,*N*-dimethylformamide (DMF) and 1 mL of 2 M HCl. The resulting solution was stirred for approximately 40 min and then transferred to a Teflon-lined stainless-steel autoclave for hydrothermal synthesis at 200 °C for 17 h using a heating rate of 5 °C $min^{-1}$. After completion, the mixture was cooled to room temperature and subjected to the same purification protocol described in Section 4.1.1, including centrifugation, washing, dialysis, and drying.

**2.1.3. Cu,N-doped CQD from glucosamine (Cu,N-GAH).** In a typical procedure, 2.1 mmol of glucosamine hydrochloride (GAH, 0.45 g) and 0.105 mmol of copper(II) acetate ($Cu(OAc)_2$, 0.02 g) were used as precursors. The reagents were dissolved in 3 mL of deionized water under stirring, followed by the dropwise addition of 2 mL of *N*,*N*-dimethylformamide (DMF) and 1 mL of 2 M HCl. The resulting solution was stirred for approximately 40 min and then transferred to a Teflon-lined stainless-steel autoclave for hydrothermal synthesis at 200 °C for 17 h with a heating rate of 5 °C $min^{-1}$. After the reaction, the autoclave was cooled to room temperature, and the resulting suspension was purified following the same procedure described in Section 4.1.1, including centrifugation, washing, dialysis, and drying.

**2.1.4. Electrode preparation.** The catalyst ink was prepared from 40 mg CQD and 10 mg ionomer PPO-LC (Fig. S1) in 400 μL of dimethylsulfoxide (DMSO), left under agitation overnight and then sonicated for 30 minutes. 2 μL of this ink was drop-casted on activated carbon paper[22] using a syringe and the electrode was dried 3 h in a rotary pump at 40 °C.

### 2.2. Characterization

**2.2.1. Raman spectroscopy.** Raman spectra were recorded using an Optosky ATR8300MP Raman Microscope with an excitation wavelength of 785 nm and a laser power of 40 mW. The power was reduced as needed by neutral density filters in order to prevent sample damage.

**2.2.2. X-ray photoelectron spectroscopy (XPS).** A drop of CQD suspension in water was deposited on a gold foil and then dried in air. Photoemission spectra were obtained using an Escalab 250Xi spectrometer (Thermo Fisher Scientific) with a monochromatic excitation source (Al Kα, 1486.6 eV). The binding energy scale was calibrated by positioning the C 1s peak of aliphatic carbon (C–C, C–H bonds) at 285.0 eV and controlling that the Fermi level corresponded to 0 eV. FWHM values used in the peak fitting procedure were of 2.3, 2.7 and 3.0 eV, correspondingly for Cu $2p_{3/2}$, N 1s and S 2p peaks. Shirley background was subtracted for XPS quantification.

**2.2.3. Scanning electron microscopy and optical microscopy.** SEM micrographs of the electrodes were recorded using a ZEISS Gemini SEM 500 at an acceleration voltage of 5 kV. The optical micrographs were collected with a Leitz Aristomet microscope.

**2.2.4. Contact angle measurements.** The water contact angle was determined with a Biolin Scientific Attension Theta Flex optical tensiometer. 3 μL of water were dropped on the surface of the electrode with a rate of 0.1 $\mu L\ s^{-1}$. The drop shape was captured immediately with the camera and the contact angle was calculated according to Young-Laplace analysis.

**2.2.5. Electrochemical measurements.** All electrochemical measurements were carried out in an H-cell using a Biologic potentiostat VMP3. The anolyte and catholyte were separated by a Nafion-211 membrane to prevent oxygen diffusion to the cathode side, which can disturb the current density measurement, and diffusion of the ECO2R products, which can undergo reoxidation at the anode side, perturbing the faradaic efficiency calculation. A three-electrode set-up was used: 0.28 $cm^2$ carbon paper with the copper-doped CQD was put on a rotating disk electrode (RDE, OrigaTrod, OrigaLys) as working electrode. Ag/AgCl with saturated KCl was used as reference electrode ($E$ = 0.197 V *vs.* SHE). Both working and reference electrodes were put in the cathodic compartment. A 2.5 cm × 2.5 cm platinum foil served as counter electrode and was placed in the anodic side. The electrolyte was 0.1 M $KHCO_3$. The volume of catholyte and anolyte was 50 $cm^3$ in each compartment.

Impedance measurements were performed by applying potentiostatic electrochemical impedance spectroscopy (PEIS) at open-circuit potential with an ac amplitude of 20 mV in a range of 1 MHz to 1 Hz. The linear sweep voltammetry (LSV) measurements were carried out at room temperature in a range of −0.6 to −1.4 V *vs.* Ag/AgCl ($\approx$0 to −0.8 V *vs.* RHE) after 40 min of $N_2$ and 40 min of $CO_2$ bubbling. Carbon dioxide was continuously injected during the experiment. The capacitance measurements were done using cyclic voltammetry in a range of −0.01 V to −0.15 V *vs.* Ag/AgCl at scan rates of 20, 40, 60, 80 and 100 mV $s^{-1}$ in $N_2$-purged 0.1 M $KHCO_3$.

The product formation and FE were studied using chronoamperometry for 2 h at potentials of 0, −0.2, −0.4, −0.6 and −0.8 V *vs.* RHE.

**2.2.6. Product analysis.** The ECO2R products were analyzed by high performance liquid chromatography (HPLC, Agilent 1260 Infinity). The column used to separate the ECO2R products was a Hi-Plex H column (Agilent Technologies) with the temperature maintained at 60 °C. The detector was a refractive index detector (RID) and its temperature was maintained at 55 °C. The eluent used for this analysis was 1 mM $H_2SO_4$. 100 μL of sample was injected during the HPLC analysis. Calibration curves for acetate (retention time: 16.2 min) and formate ions (retention time: 14.5 min) were determined (Fig. S2); several other molecules (methanol, ethanol, propanol, acetaldehyde . . .) were examined, but not detected in our samples. The limits of detection (LOD) by HPLC were 2 $\mu mol\ L^{-1}$ for acetic acid and 1 $\mu mol\ L^{-1}$ for formic acid. Additional attempts to detect CO were performed by adsorption of the gas phase on a high-affinity zeolite trap followed by thermal desorption and GC analysis. Under the applied potentials, no CO was detected within the instrumental detection limit. Moreover, hydrocarbon products such as $CH_4$ and $C_2H_4$ were not observed. Furthermore, several catholyte samples were also analysed by hydrogen nuclear magnetic resonance spectroscopy ($^1$H-NMR, 700 MHz, Bruker) with $D_2O$ as internal lock (Fig. S3). The concentrations were detected with an internal standard dimethylformamide and the analysis was confirmed by calibration with known concentrations of acetate (Fig. S4 and Table S1). The LOD were 1–10 $\mu mol\ L^{-1}$ for acetic acid and 5–20 $\mu mol\ L^{-1}$ for formic acid.

## 3. Results

### 3.1. Synthesis and spectroscopic characterization

The formation process of heteroatom-doped CQD is represented schematically in the Fig. 1. The atomic positions are identified by XPS, as shown below.

Fig. 2 shows the Cu 2p, S 2p, and N 1s XPS spectra of the CQD samples. Table 1 compares the atomic composition of the precursor solutions (in at%), calculated from the quantity and chemical composition of the starting materials, with the corresponding elemental composition of the resulting CQDs as determined by XPS analysis.

Whereas the carbon content reflects globally the composition of the precursor solutions, interesting trends emerge for

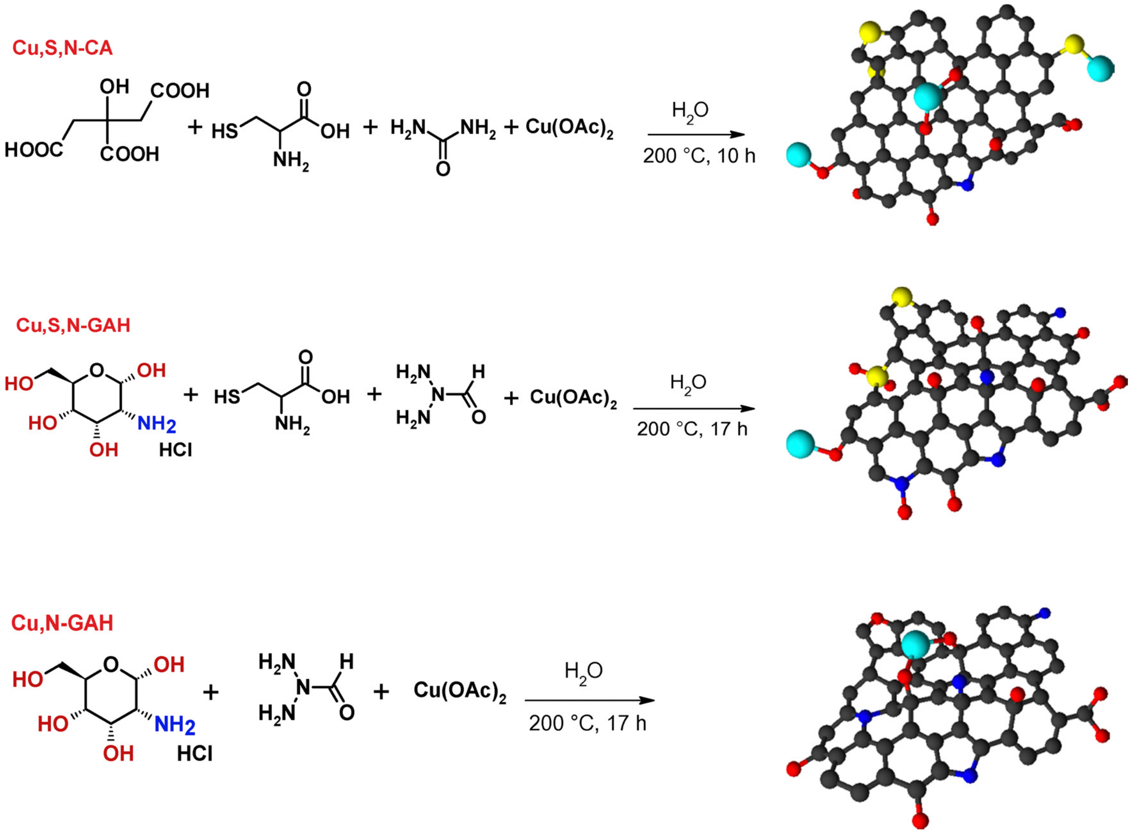

Fig. 1 Schematic formation process and composition of CQD. Black: carbon, red: oxygen, blue: nitrogen, yellow: sulfur, light blue: copper.

the other components. For the sample prepared from citric acid, the oxygen content in the resulting CQD is much lower than in the precursor solution, presumably because a large fraction of oxygen was lost in condensation reactions in the form of water. This finding is in agreement with the low content of C 1s B and O 1s B (see Table 2), related *inter alia* to C–O bonds. However, the O/C ratio in Cu,S,N-CQD-CA is still much higher than in the other samples, increasing its hydrophilicity[24] and presumably enhancing the HER activity. By contrast, the oxygen content of CQD derived from glucosamine is comparable to that of the precursor solution.

Nitrogen consistently decreases in the CQD compared to their precursors; the loss can be attributed to the release of ammonia during the synthesis. The higher nitrogen content in GAH-based samples arises from the larger variety of nitrogen sources present, including beyond glucosamine also cysteine and DMF. Copper and sulfur, in contrast, are significantly enriched in the CQD relative to their precursor concentrations with an increase by a factor of about 5 for sulfur and about 15 for copper. The particular high copper content in Cu,S,N-CQD-CA is certainly related to the strong chelating ability of citric acid, which is known to coordinate copper ions and is used in citrate-based synthesis routes.[27]

Table 2 presents a summary of the chemical states of the various elements. Some peculiar features can be further discussed.

The predominance of the Cu(I) oxidation state (above 80%) in the CA-based sample can be attributed to the reducing environment provided by citric acid. In Cu,S,N-CQD-GAH, Cu(II) is partially reduced by cysteine, whereas in the absence of cysteine (Cu,N-CQD-GAH) Cu(II) remains the only oxidation state detected.[28]

Concerning the oxidation state of sulfur, only thioether form is observed in the CA-based sample in accordance again with reducing conditions during the hydrothermal synthesis, whereas various oxidation states of sulfur are detected in sample Cu,S,N-CQD-GAH.

As many publications on ECO2R mentioned that pyridinic nitrogen plays an important role in enhancing electrocatalytic performance compared to other types of nitrogen, a deeper analysis was made using the XPS data. According to the work of Lazar *et al.* on spectroscopic fingerprints of graphitic, pyrrolic, and pyridinic nitrogen in N-doped graphene,[31] we categorized the N-dopants found in our electrocatalysts according to their N 1s binding energy. GAH-based samples present a significantly higher content of aminic/pyrrolic nitrogen than sample Cu,S,N-CQD-CA. Furthermore, sample Cu,S,N-CQD-GAH contains also some nitrogen on pyridinium oxide positions. Graphitic nitrogen, known to be formed by condensation reaction of the precursor glucosamine (pyrazine formation), is observed only in sample Cu,N-CQD-GAH in low concentration.

Fig. 3 displays the Raman spectra of the CQDs, highlighting the characteristic G and D bands. The position of the G band is known to shift depending on the degree of disorder in the carbonaceous material, typically ranging from approximately

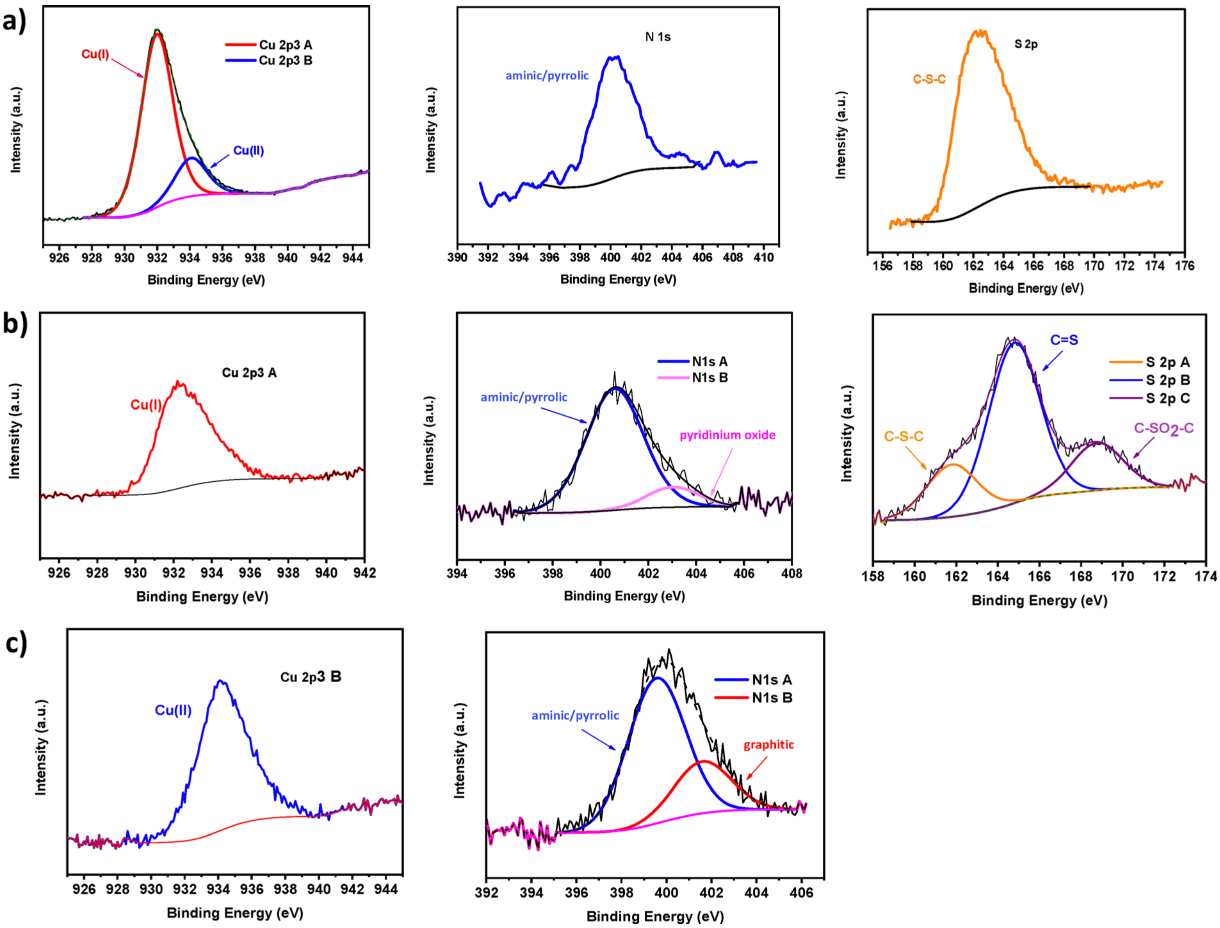

Fig. 2 X-Ray photoelectron spectra (Cu 2p, S 2p and N 1s). (a) Cu,S,N-CQD-CA, (b) Cu,S,N-CQD-GAH, (c) Cu,N-CQD-GAH.

Table 1 Comparison of atomic composition of precursor solutions and CQD by XPS

| | Cu,S,N-CA | | Cu,S,N-GAH | | Cu,N-GAH | |
|---|---|---|---|---|---|---|
| Composition/at% | Solution | CQD | Solution | CQD | Solution | CQD |
| C | 45.6 | 47.1 | 57.6 | 62.5 | 58.2 | 68.4 |
| O | 45.0 | 23.0 | 24.0 | 23.0 | 23.7 | 18.1 |
| N | 5.3 | 1.9 | 17.7 | 4.7 | 17.9 | 5.3 |
| S | 3.0 | 14.8 | 0.9 | 5.6 | — | — |
| Cu | 0.6 | 7.1 | 0.1 | 1.6 | 0.1 | 1.5 |

1590–1600 cm$^{-1}$ in nanocrystalline graphite down to around 1520 cm$^{-1}$ in amorphous carbon.[32] This shift is attributed to factors such as the clustering of sp$^2$ domains, bond disorder, the presence of sp$^3$-hybridized carbon atoms, and their interaction with aromatic domains.[32] The different components within this spectral region can be associated with disordered graphitic structures.

The D band, commonly centered around 1350 cm$^{-1}$, is a disorder-induced band that becomes Raman-active in the presence of structural defects. Its presence is often linked to the incorporation of heteroatoms, such as oxygen, nitrogen, and sulfur. Although Raman spectra are significantly influenced by these heteroatoms, the quantitative attribution of their individual contributions remains challenging. For instance, in the case of nitrogen, several models have been proposed to interpret its impact on Raman features; however, their applicability is limited when the nitrogen concentration falls below 10%.[31,33]

The intensity ratio between the D and G bands ($I_D/I_G$) is commonly used as an indicator of the defect density within the carbon structure. Specifically, the $I_D/I_G$ values are 1.39 (Cu,S,N-CQD-CA), 1.43 (Cu,S,N-CQD-GAH), and 1.13 (Cu,N-CQD-GAH). Nevertheless, the D and G bands may reflect not only graphitic domains and structural defects but also the presence of polyaromatic ring systems of varying sizes. Specifically, the D band in the 1380–1400 cm$^{-1}$ region has been associated with fused aromatic rings, while the G band around 1520–1550 cm$^{-1}$ has been linked to aromatic ring breathing modes. By comparing the three spectra shown in Fig. 3, it is observed that sample Cu,N-CQD-GAH exhibits a higher intensity of the G band, which suggests an increase in the number or size of graphene domains.[34] This enhancement may also correlate with the lower content of heteroatoms (no sulfur) further indicating improved structural ordering in the sample.

A typical SEM micrograph of electrode sample Cu,S,N-CQD-GAH is shown in Fig. 4. One can notice the fibers of carbon paper and the porous electrode structure; the CQDs are too

Table 2 Chemical state of various elements in CQD

| Peak | BE, eV | Cu,S,N-CQD-CA at% | Cu,S,N-CQD-GAH at% | Cu,N-CQD-GAH at% | Chemical state |
|---|---|---|---|---|---|
| C 1s A | 285.0 | 31.6 | 24.6 | 38.0 | C–C, C–H, C═C (graphite[29]) |
| C 1s B | 286.3–287.1 | 7.3 | 28.9 | 23.7 | C–O, C═N |
| C 1s C | 288.2–290.0 | 8.2 | 9.0 | 6.7 | C═O |
| O 1s A | 531.7 | 14.9 | 12.6 | 3.1 | C═O aromatic, –OH |
| O 1s B | 533.5–534.0 | 4.5 | 7.9 | 12.6 | C–O |
| O 1s C | 535.7–536.1 | 3.6 | 2.5 | — | C═O carboxylic acid |
| O 1s D | 537.4 | — | — | 2.4 | C–O–C aromatic |
| N 1s A | 399.6–400.6 | 1.9 | 4.1 | 3.9 | Aminic/pyrrolic |
| N 1s B | 401.6 | — | — | 1.4 | Graphitic |
| N 1s C | 403.0 | — | 0.6 | — | Pyridinium oxide $N^+–O^-$ |
| S 2p A | 161.8–162.3 | 14.8 | 1.1 | — | C–S–C |
| S 2p B | 164.8 | — | 3.5 | — | C═S[30] |
| S 2p C | 168.8 | — | 1.0 | — | $C–SO_2–C$ |
| Cu $2p_3$ A | 932.0–932.3 | 5.8 | 1.6 | — | $Cu_2O$, $Cu_2S$ |
| Cu $2p_3$ B | 934.1 | 1.3 | — | 1.5 | CuO |

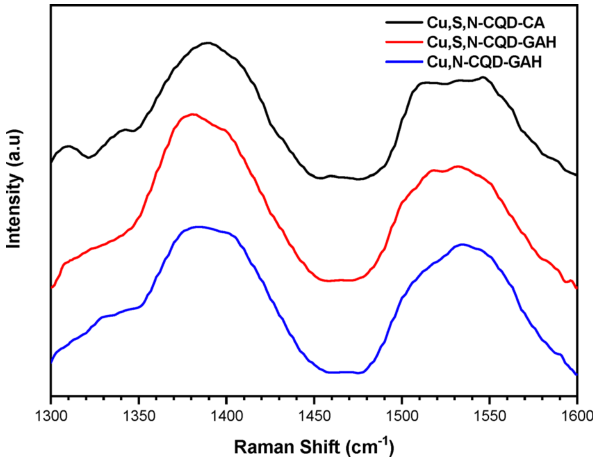

Fig. 3 Raman spectra of heteroatom-doped CQD.

small to be observed. SEM images of the other samples and representative optical micrographs of all electrodes are reported in the SI (Fig. S5 and S6).

### 3.2. Electrochemical $CO_2$ reduction

Capacitance measurements for the electrodes by cyclovoltammetry are reported in Fig. 5 and Fig. S7.

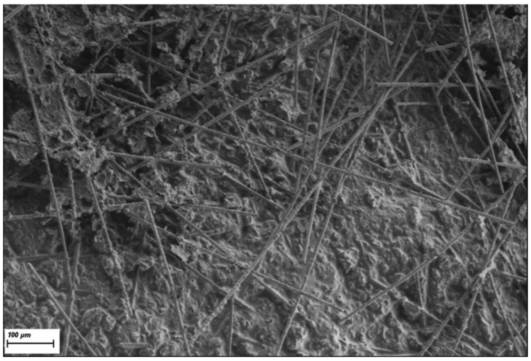

Fig. 4 Typical scanning electron micrographs of a Cu,S,N-CQD-GAH electrode.

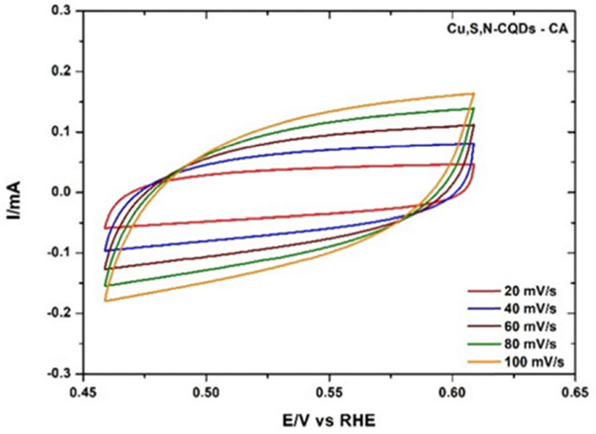

Fig. 5 Cyclovoltammograms of Cu,S,N-CQD-CA in 0.1 M $KHCO_3$ at various scan rates.

The capacitance $C$ can be obtained from the current $j$ at various scan rates $dU/dt$, according to the equation:

$$j = C \times \frac{dU}{dt} \tag{1}$$

The resulting average values are reported in the SI (Table S2). Typical impedance spectra of the samples are also reported in Fig. S8 together with the best-fit parameters (Table S2).

The data of capacitance $C$ and CPE Q3 are consistent and show relatively similar ECSA for all samples. Assuming a typical double layer capacity of carbonaceous materials of 20 μF cm$^{-2}$, an electrochemically active surface area (ECSA) between 60 and 95 cm$^2$ can be calculated from the capacitance values; using the geometric electrode area (0.28 cm$^2$), a roughness factor in the range 220–330 is found. These relatively high ECSA values are expected to improve the electrocatalytic performance of the electrodes.

Fig. 6 presents the linear sweep voltammograms (LSV) of the Cu-doped CQD electrocatalysts on carbon paper.

Every measurement was repeated at least 7 or 8 times to verify the reproducibility. An example of repeated LSV curves is shown in the SI (Fig. S9). The LSV are gradually dominated

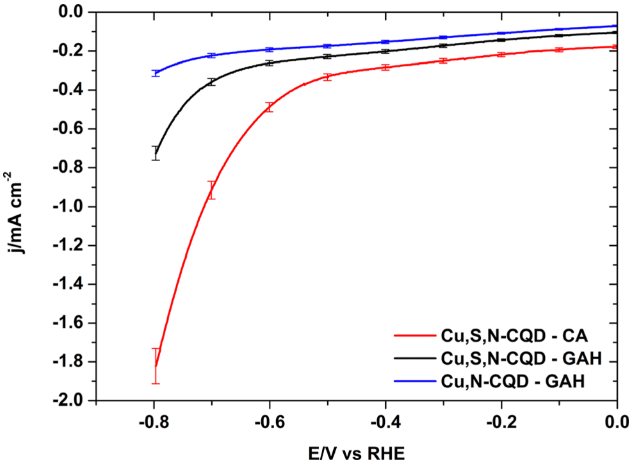

Fig. 6 Linear sweep voltammograms of Cu-doped CQD electrocatalysts in $CO_2$-saturated 0.1 M $KHCO_3$ at 2500 RPM.

below $E = -0.4$ V per RHE by the HER with a current density in the order: Cu–S–N-CQD-CA > Cu–S–N-CQD–GAH > Cu–N-CQD-GAH. In order to understand this behaviour, water contact angle measurements were performed on the electrodes. The sessile drop shapes are shown in the SI (Fig. S10) and the contact angles are reported in Table 3.

There is a clear correlation between the hydrophilicity of the electrodes and the amount of HER. Cu,S,N-CQD-CA presents a too high hydrophilicity attributable to the precursor citric acid, known to give hydrophilic CQD, and the high content of copper ions, which has to be avoided as it enhances the competitive HER.

Typical chronoamperograms at various potentials between 0 and −0.8 V per RHE are presented in Fig. 7.

All chronoamperometric measurements were repeated several times to ensure reproducibility, and the error bars represent the standard deviation of the steady-state current densities. The higher current density observed at −0.8 V *vs.* RHE, particularly for sample A (Fig. 7a), is attributed to the enhanced hydrogen evolution reaction (HER) at more negative potentials. The pronounced hydrophilicity of sample A facilitates proton transport to the electrode surface, thereby promoting HER and increasing the total current. The noisier chronoamperometric response observed for sample C (Fig. 7c) at −0.4 V is likely caused by gas bubble nucleation and detachment during HER, which temporarily block active sites and induce transient current fluctuations. The quantitative analysis of the products by HPLC showed only acetate and formate ions (Fig. S8). To confirm these results by an independent method, $^1$H NMR spectra were also registered. A typical $^1$H-NMR spectrum (Fig. S9) confirmed the presence of acetate and formate; no other products were identified. A quantitative analysis of acetate by NMR is reported in Fig. S10 and compared with the values detected by HPLC (Table S2). Attempts to determine a possible amount of CO by gas chromatography were unsuccessful, including direct injection with a syringe, but also by thermal desorption after previous adsorption in a zeolite with high CO affinity. Tonelli and coworkers also found no CO at low cathodic potential (−0.4 V *vs.* RHE) and only $H_2$ was detectable for all tested copper-based catalysts.[12]

Table 3 Cathodic current *j*, water contact angles and content and oxidation state of copper

| Sample | *j*/mA cm$^{-2}$ at $E = -0.7$ V per RHE | Water contact angle (±10°) | Cu content (at%) and redox state |
|---|---|---|---|
| Cu,S,N-CA | −0.99 | 27 | 7.1 Cu(I/II) |
| Cu,S,N-GAH | −0.40 | 61 | 1.6 Cu(I) |
| Cu,N-GAH | −0.23 | 85 | 1.5 Cu(II) |

In $CO_2$-saturated 0.1 M $KHCO_3$ solution (pH ≈ 7), the ECO2R to formate and acetate ions can be expressed by the following chemical equations and standard potentials *vs.* the reversible hydrogen electrode (RHE).[7,17]

$$CO_2 + H_2O + 2e^- \rightarrow HCOO^- + OH^- \quad E^\circ/\text{RHE} = -0.02\ \text{V}$$

$$2CO_2 + 5H_2O + 8e^- \rightarrow CH_3COO^- + 7OH^- \quad E^\circ/\text{RHE} = 0.11\ \text{V}$$

The faradaic efficiency is defined by the relation with Faraday's constant $F$ (96 485 C mol$^{-1}$), the molar quantity of a specific product $n$, the number of exchanged electrons $z$ and the total charge $Q$:[6]

$$\text{FE} = \frac{n \times z \times F}{Q} \tag{2}$$

The FE for acetate and formate are also shown in Fig. 7. A FE = 86.6% for acetate formation is observed for Cu,S,N-CQD-CA at −0.4 V per RHE. For Cu,S,N-CQD-GAH, the FE for acetate formation is above 45% for all potentials between 0 and −0.4 V per RHE with a maximum of 66.8% at −0.2 V per RHE; a maximum FE = 31.3% is observed for formate at −0.2 V per RHE. One should however keep in mind that the FE is biased when comparing acetate and formate, due to the lower number of transferred electrons for formate ($z = 2$) than for acetate ($z = 8$), which reduces the FE for the former.

For that reason, the production rates, normalized by the amount of catalyst, calculated from eqn (3) are more significant. The area-specific productivity $r$ (mol h$^{-1}$ cm$^{-2}$) of a compound can be calculated from the overall cathodic current density $j$ and the FE according to the equation:

$$r = \frac{\text{FE} \times j}{z \times F} \tag{3}$$

It can be also expressed as function of the mass of electrocatalyst (mol h$^{-1}$ $g_{cat}{}^{-1}$). The catalyst mass-specific acetate and formate production rates are reported in Fig. 8.

One can observe bell-shaped curves showing the highest production rate for acetate for all samples at −0.4 V per RHE; for formate, the highest rates are also observed at −0.4 V per RHE, except for sample Cu,S,N-CQD-GAH at −0.2 V per RHE. Such curves can be understood by the fact that the catalytic reaction starts at a certain onset potential; the partial current increases then exponentially with the overpotential, according to the Butler–Volmer equation, until diffusion limitations occur and the onset of the competing HER block catalytic sites for the ECO2R and the product formation rate decreases.

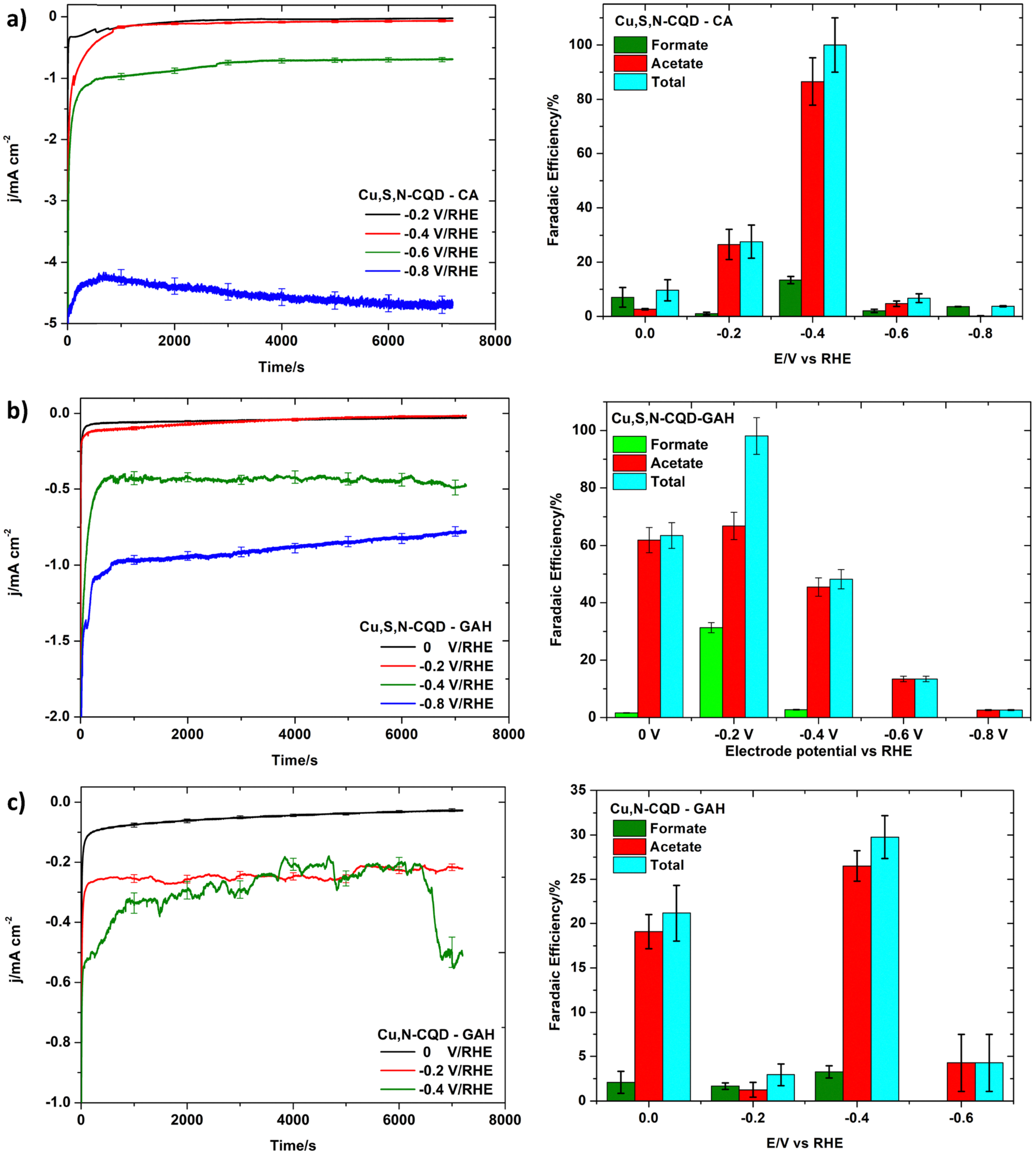

Fig. 7 Chronoamperograms and faradaic efficiencies of (a) Cu,S,N-CQD-CA, (b) Cu,S,N-CQD-GAH, and (c) Cu,N-CQD-GAH at 2500 rpm and various electrode potentials.

The maximum production rate of acetate at −0.4 V per RHE for sample Cu,S,N-CQD-GAH, $r$ = 1.53 mmol $g_{cat}{}^{-1}$ $h^{-1}$, is the highest reported value in the literature at such low overpotential (Table 4). The maximum formate production rate at −0.2 V per RHE, 0.6 mmol $g_{cat}{}^{-1}$ $h^{-1}$, is slightly lower than corresponding literature data.[12]

Some other very recent data on faradaic efficiency and ECO2R current densities of doped carbonaceous materials can be found in Table 5.

The energy efficiency (EE) for a specific product can be expressed as function of the thermodynamic cell voltage $\Delta E$, the overpotential $\eta$, and the faradaic efficiency FE:[6,10]

$$\mathrm{EE} = \mathrm{FE} \times \frac{\Delta E}{\Delta E + \eta} \tag{4}$$

The half-cell EE takes only the overpotential of the cathodic reaction into account. An interesting feature of the electrocatalyst Cu,S,N-CQD-GAH is the low overpotential at which the

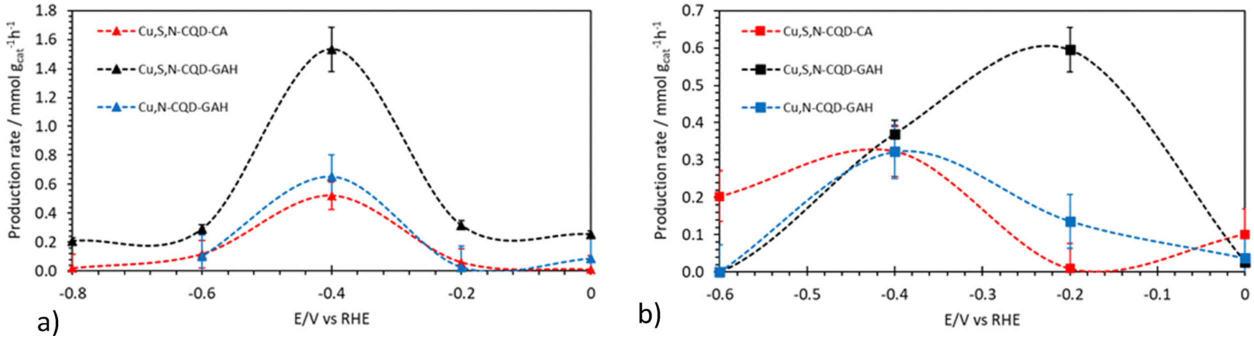

Fig. 8 Production rates of (a) acetate and (b) formate ions, normalized by the amount of catalyst.

Table 4 Comparison of acetate and formate production rates *r* and FE with the literature

| | Formate | | | Acetate | | |
|---|---|---|---|---|---|---|
| Electrodes | *E*/V *vs.* RHE | *r*/mmol $g_{cat}^{-1}$ $h^{-1}$ | FE/% | *r*/mmol $g_{cat}^{-1}$ $h^{-1}$ | FE/% | Ref. |
| Cu,S,N-CQD-GAH on carbon paper | −0.2 | 0.60 | 31.3 | 0.32 | 66.8 | This work |
| | −0.4 | 0.37 | 2.8 | 1.53 | 45.5 | |
| $Cu_2O$/Cu on carbon paper | −0.4 | 0 | 0 | 0.31 | 76 | 12 |
| Dendritic $Cu_2O$/Cu | −0.4 | — | 0 | — | 48 | 13 |
| $Cu_2O$ on carbon paper | −0.85 | — | 8.1 | — | 0.5 | 35 |
| Cu nanoparticles | −0.9 | — | 40 | — | <1 | 36 |

Table 5 Literature values for various doped carbon materials

| Electrocatalyst | Electrolyte | Cell | Main products (FE and/or *r*) | Ref. |
|---|---|---|---|---|
| Hydrophobic CQDs with high Lewis-basic nitrogen sites | 1 M KOH | Flow cell | $CH_4$ FE = 52% at −2.0 V per RHE<br>$j_{CH_4}$ = 178 mA $cm^{-2}$ | 37 |
| Bifunctional CQD-embedded MOF nanohybrids | 0.1 M NaOH | H-cell | CO FE = 91% at −0.64 V per RHE<br>*j* = 50 mA $cm^{-2}$ | 38 |
| Atomic-Fe-rich CQDs | 1 M KOH | Flow cell | CO FE = 92% at −0.53 V per RHE<br>$j_{CO}$ = 402 mA $cm^{-2}$ | 39 |
| Copper single atoms decorated N-doped CQDs | 0.1 M $KHCO_3$ | H-cell | $C_2H_5OH$ FE = 70% at −0.2 V per RHE<br>*j* = 1.0 mA $cm^{-2}$ | 11 |
| Municipal sludge-derived CQD decorated, N-doped hierarchical biocarbon | 0.1 mol $L^{-1}$ $KHCO_3$ | Gas-tight one compartment cell | $C_2H_5OH$, $CH_3OH$, and $CH_4$<br>Total FE = 90.1% at −0.71 V per RHE<br>$rC_2H_5OH$ = 111.1 μg $h^{-1}$ $cm^{-2}$<br>$rCH_3OH$ = 35.7 μg $h^{-1}$ $cm^{-2}$<br>$rCH_4$ = 16.8 μg $h^{-1}$ $cm^{-2}$<br>*j* = 18.5 mA $cm^{-2}$ at −1.01 V per RHE | 40 |
| Single copper atoms anchored on N,P co-doped carbon with carbonization temperature of 800 °C | 0.1 M $KHCO_3$ | H-cell | FE at −1.19 V per RHE<br>CO (FE = 6.9%); $CH_4$ (FE = 1.7%)<br>$C_2H_4$ (FE = 20.8%); $C_2H_5OH$ (FE = 13.5%); $C_3H_7OH$ (FE = 5.9%)<br>*j* = 21.4 mA $cm^{-2}$ | 41 |
| Cu-decorated N-doped carbon nanosheets | 0.5 M $KHCO_3$ | H-cell | Acetate FE ≈ 16% at −0.8 V per RHE | 42 |
| $sp^2$/$sp^3$ hybrid carbon | 0.1 M $KHCO_3$ | H-cell | Acetate FE ≈ 62.7% at −0.8 V per RHE | 43 |

production rates are observed and consequently a high energy efficiency: at −0.2 V per RHE, $\eta$ = −0.18 V for formate and −0.31 V for acetate. The half-cell EE can be calculated according to eqn (4), which gives with the FE of Table 4 for formate EE = 27.4% and for acetate EE = 52.3%. These values are quite high, especially for acetate, and among the best in the literature.[10]

The stability of the electrocatalyst is another figure of merit, which can be evaluated by accelerated degradation tests using either cyclovoltammetry or chronoamperometry. We made accelerated degradation tests using chronoamperometry. Fig. 9 shows a chronoamperogram of Cu,S,N-CQD-GAH in $CO_2$-saturated 0.1 M $KHCO_3$ solution at −0.4 V per RHE. The large decrease of the current over the initial period, until approximately 3 h, was described before[12] and can be attributed to the reduction of the copper catalyst (catalyst activation) and a progressive decrease of the HER in the $CO_2$-saturated solution. After 3 h, the current stabilized and further decrease

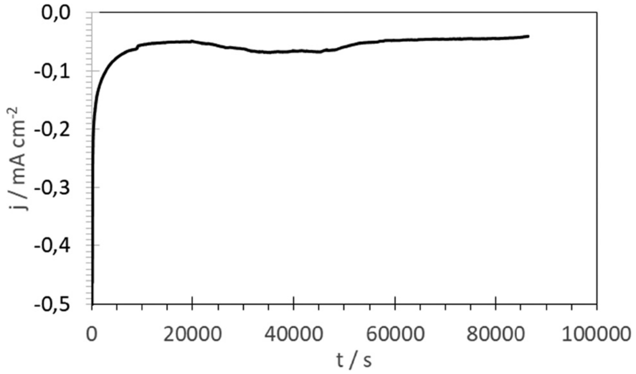

Fig. 9 Chronoamperometric long-time test of Cu,S,N-CQD-GAH at −0.4 V per RHE in $CO_2$-saturated 0.1 M $KHCO_3$.

of current density over time was low (10%) and attributable to various factors, including poisoning by impurities from the experimental set-up, such as metallic contaminants, poisoning by irreversibly adsorbed reaction intermediates,[9] and restructuring of the catalyst surface during the electrochemical reaction.[2]

Fig. 10a compares the FTIR spectra of the electrodes before and after linear sweep voltammetry (LSV) and chronoamperometry (CHR). Overall, the spectra exhibit similar general features; however, distinct variations appear across several wavenumber regions, reflecting changes in surface chemistry after electrochemical operation. A new band at $\approx 1000$ cm$^{-1}$ emerges after both LSV and CHR, consistent with the formation of oxygenated $CO_2$-reduction products such as formate or carbonate. The persistence of this band after CHR suggests stabilization of $CO_2$-derived groups on the catalyst surface under reducing conditions.

The band at $\approx 1110$ cm$^{-1}$, assigned to C–O (or C–N) stretching vibrations of oxygenated surface groups, is already present in the pristine catalyst and increases after LSV, indicating the generation of additional surface functionalities. After CHR, this band disappears, implying further reduction or desorption of these species during prolonged polarization A band near 1185 cm$^{-1}$, initially weak in the pristine sample, becomes intense after CHR and is eliminated following LSV. This behaviour suggests accumulation of surface-bound oxygenated species, plausibly organic C–O groups, formed under extended polarization and removed or transformed during the cathodic potential sweep. The band at $\approx 1370$ cm$^{-1}$ becomes more intense after both LSV and CHR, indicating the formation of surface carboxylate or carbonate/bicarbonate species. This feature corresponds to the symmetric stretching of $CO_2$-derived adsorbates that accumulate during electrochemical reduction. Finally, the band at $\approx 1640$ cm$^{-1}$ increases markedly in intensity after electrochemical test. This vibration is attributed to the H–O–H bending mode of physically adsorbed or interlayer water, consistent with increased surface hydration of the electrode after immersion in electrolyte solution.

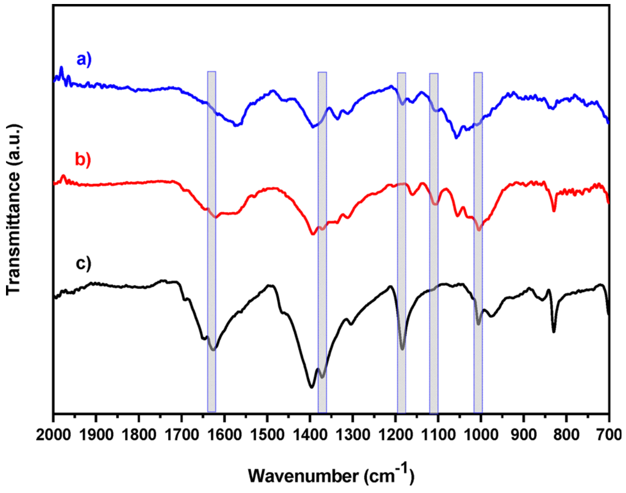

Fig. 10 FTIR spectra of: (a) Cu,S,N-CQD-CA, (b) Cu,S,N-CQD-CA after linear sweep voltammetry, (c) Cu,S,N-CQD-CA after chronoamperometry.

## 4. Discussion

Formate and acetate ions are two useful products of the ECO2R. Formic acid is a promising liquid fuel with considerable energy density and an efficient hydrogen carrier for direct formic acid fuel cells (DFAFC).[44,45] Furthermore, it is widely used in several industries, *e.g.* as coagulant for rubber, as antibacterial agent in livestock feed,[45] for tanning and leather.[46] Acetic acid, beyond its role in vinegar and bio-oils for hydrogen production,[46] is a crucial feedstock for many industrial processes and derivatives, such as acetic anhydride, vinyl acetate, which are important intermediates in organic synthesis, polymers, medicine, and agriculture. Acetic acid can be also converted biochemically into other value-added complex chemicals, such as fatty acids.[47]

The electrocatalytic mechanisms of ECO2R are not well understood, although many theoretical attempts, especially by DFT approaches,[1,6,7,10,48] were reported. There is only consensus on the first two steps: the $CO_2$ adsorption on the catalyst surface and the one-electron reduction of $CO_2$ to the radical anion $^{\bullet}CO_2^{-}$ as the following slow step.[6,9,16,17,49] In the case of formate, a single rapid protonation/reduction step of $^{\bullet}CO_2^{-}$ leads to the product.[6,45] The mechanism of C–C coupling, leading *e.g.* to acetate, is more complicated and still a matter of debate.[47] According to many authors, it involves the formation of adsorbed *CO, obtained from the radical anion by a second electron/proton transfer and following water loss,[6] which dimerizes at the electrode surface into an adsorbed *OC–CO species;[7] after this C–C coupling, considered rate-determining,[10] further electron and proton transfer steps lead to the formation of the final product. However, alternative key intermediates were also proposed: (i) adsorbed *$CH_3$,[7] formed by multiple reduction/protonation steps from $^{\bullet}CO_2^{-}$; (ii) adsorbed oxalate formed by dimerization of $^{\bullet}CO_2^{-}$.[18]

The catalyst performance depends strongly on precursor chemistry and surface composition. The most hydrophilic sample, made from citric acid, is giving mostly hydrogen evolution and a relatively low amount of ECO2R products due to the high O/C ratio and the high content of copper ions introduced by the interaction with citrate (Table 1). The use of glucosamine reduces the hydrophilicity and leads to a lower percentage of copper ions. Indeed, hydrophobic electrode surfaces can trap appreciable amounts of nanoscale gas bubbles inside an aqueous electrolyte,[50] which enables $CO_2$ accumulation at the catalyst/solution interface.

Adsorption and activation of $CO_2$ at the initial stage were reported to be the most decisive factors for the ECO2R.[8] An enhancement of surface forces with the highly inert $CO_2$, *e.g.* by acid–base interactions[45] or by the presence of heteroatoms that form local dipoles, enhances the adsorption of $CO_2$ and is beneficial for the ECO2R. There is a significantly higher amount of nitrogen on aminic positions in GAH-based samples (4.1 and 3.9 at%, respectively); Cu,S,N-CQD-GAH contains also a small amount of pyridinium oxide (Table 2). The free electron pair of Lewis base amine groups[49] and the polar $N^+O^-$ bond of pyridinium oxide facilitate the adsorption of molecules like $CO_2$ improving the initial adsorption step of the ECO2R. Furthermore, sulfur doping of carbonaceous materials was also reported to have a beneficial effect on $CO_2$ adsorption and the formation of the $^*CO_2^-$ key intermediate.[51] In fact, Cu,S,N-CQD-GAH gave the highest production rates for both acetate and formate.

Concerning the contribution of copper in the electrocatalytic process, Cu metal surfaces have a positive adsorption energy for hydrogen, but a negative one for *CO,[1] so that they are able to chemisorb $^\bullet CO_2^-$ radical anions and *CO species,[4] which are key intermediates of the electrocatalytic $CO_2$ conversion. $Cu^+$ ions show also a high affinity for CO, as illustrated by the strong copper(I)carbonyl complexes $[Cu(CO)_n]^+$ in aqueous solution.[52] Assuming that *CO dimerization is the key step for the selective conversion of $CO_2$ to acetic acid, this process requires a longer residence time than the process necessary for the $C_1$ pathway, which produces $HCOO^-$.[12] The CO chemisorption promotes not only the C–C coupling reaction, but also saturates the reaction sites for the parasitic HER. These considerations support the ECO2R mechanism by adsorbed *OC–CO intermediates.

The catalytic productivity and selectivity toward formic and acetic acids depend on the electrocatalyst morphology and the Cu oxidation state. Tonelli and coworkers studied copper-based catalyst with various copper oxidation states and showed that $Cu_2O$/Cu composites presented the highest rate of formation of acetate, whereas Cu(II) oxides gave a lower amount of acetate and a higher quantity of hydrogen.[12] A mixed $Cu_2O$/Cu catalyst made by electrodeposition of Cu metal on a carbon support had a high selectivity (76% FE) for acetic acid at a relatively low potential (−0.4 V *vs.* RHE). A dendritic Cu/$Cu_2O$ composite electrode gave also a high FE for $C_2$ products and acetate.[13] The presence of $Cu_2O$ was also found to be important for the formation of $C_{2+}$ products with a high faradaic efficiency (80%) for acetic acid using electrochemically synthesized Cu/$Cu_2O$ at a potential as low as −0.4 V *vs.* RHE.[53]

The copper content in GAH-based samples is quite similar (1.6 *vs.* 1.5 at%), but the copper oxidation state (+1 *vs.* +2) is different (Table 2). The highest acetate and formate productivities observed for Cu,S,N-CQD-GAH, which contains only copper(I), are in good accordance with these findings. The ratio of $Cu^+$/Cu surface species is fundamental to boost selectivity towards $C_{2+}$ products.[8] From a mechanistic point of view, Cu(I) and Cu(0) coexisting at the electrocatalyst surface promote enhanced *CO dimerization and therefore the formation of $C_{2+}$ products, due to the negative adsorption enthalpy for CO.[48] The *in situ* reduction of a part of $Cu^+$ into Cu(0) was observed previously at the beginning of the experiments; the HER strongly dominated for metallic Cu alone.[12]

The enhanced acetate selectivity can be finally rationalized by the cooperative action of $Cu^+$, nitrogen functionalities, and sulfur dopants. Stabilized $Cu^+$ centers provide sites with suitable *CO binding strength and geometric flexibility for C–C coupling, consistent with DFT studies showing lowered barriers for $C_2$ oxygenates on Cu(I)-rich surfaces.[54] Nitrogen species (aminic or pyridinic) increase local basicity and stabilize early intermediates such as $^*CO_2^-$ and *CHO through electron donation and hydrogen-bonding interactions, as widely reported for N-doped carbon catalysts.[55] Sulfur dopants further modulate the electronic structure, introducing defect sites that tune *CO adsorption energies and promote surface mobility required for C–C coupling.[56] The combined action of these three components provides a plausible explanation for the significantly higher ECO2R activity of Cu,S,N-CQD-GAH and especially the better production rate for acetate combined with a high energy efficiency.

## 5. Conclusions

The electrochemical $CO_2$ reduction holds great promise as a sustainable technology for addressing climate change by use of $CO_2$ as a feedstock for the production of chemicals and fuels. However, to become commercially viable on a large scale, challenges related to catalyst development need to be overcome. In this work, we studied the synthesis of heteroatom-doped CQD by a hydrothermal process, employing abundant, non-toxic, and inexpensive precursors, such as citric acid, glucosamine, cysteine, and urea. Combined with a long-chain anion exchange ionomer, the resulting CQD-based electrodes were tested for their performance in $ECO_2R$.

Samples made from citric acid show an excessive hydrophilicity, also related to an elevated copper ion content, and favour the hydrogen evolution reaction. The better activity and high selectivity of Cu,S,N-CQD-GAH from glucosamine can be attributed to a combination of the following features: a high electrochemically active surface area of the electrodes, providing abundant sites for $CO_2$ activation; a suitable nitrogen content, particularly in aminic and pyridinium oxide positions, facilitating $CO_2$ adsorption; a proper quantity of $Cu^+$ species, favoring C–C coupling and enhancing acetate formation; and the presence of sulfur in various oxidation states, further improving catalytic activity.

The catalyst mass-specific production rate of acetate (1.5 mmol $g^{-1}$ $h^{-1}$) exceeds the data reported in the literature. The faradaic efficiency is consistently higher than 45% in a large range of potentials between 0 and −0.4 V per RHE and reaches 66.8% at −0.2 V per RHE. A faradaic efficiency of 31.3% is attained for formate. Furthermore, the energy efficiency is also quite high, given the low overpotential: at −0.2 V per RHE it attains 27.4% for formate and 52.3% for acetate, one of the highest values in the literature. The stability test of the catalyst by a 24 h chronoamperometric experiment shows only a low catalyst degradation after the initial activation time.

Altogether, these results highlight the effectiveness of Cu,S,N-doped CQDs synthesized from glucosamine as a promising class of electrocatalysts for $ECO_2R$. The combination of low-cost, environmentally benign precursors with high selectivity toward acetate, high energy efficiency, and promising durability makes this approach particularly attractive for advancing the practical implementation of electrochemical $CO_2$ reduction technologies.

## Conflicts of interest

There are no conflicts of interest to declare.

## Data availability

The data supporting this article have been included as part of the supplementary information (SI). Supplementary information is available. See DOI: **https://doi.org/10.1039/d5qm00916b**.

## References

1 X. She, Y. Wang, H. Xu, S. Chi Edman Tsang and S. Ping Lau, Challenges and Opportunities in Electrocatalytic CO(2) Reduction to Chemicals and Fuels, *Angew. Chem., Int. Ed.*, 2022, **61**, e202211396.

2 S. Nitopi, E. Bertheussen, S. B. Scott, X. Liu, A. K. Engstfeld, S. Horch, B. Seger, I. E. L. Stephens, K. Chan, C. Hahn, J. K. Nørskov, T. F. Jaramillo and I. Chorkendorff, Progress and Perspectives of Electrochemical $CO_2$ Reduction on Copper in Aqueous Electrolyte, *Chem. Rev.*, 2019, **119**, 7610–7672.

3 Y. Lei, Z. Wang, A. Bao, X. Tang, X. Huang, H. Yi, S. Zhao, T. Sun, J. Wang and F. Gao, Recent advances on electrocatalytic $CO_2$ reduction to resources: target products, reaction pathways and typical catalysts, *Chem. Eng. J.*, 2023, **453**, 139663.

4 Z. Gao, J. Li, Z. Zhang and W. Hu, Recent advances in carbon-based materials for electrochemical $CO_2$ reduction reaction, *Chin. Chem. Lett.*, 2022, **33**, 2270–2280.

5 A. S. Varela, W. Ju and P. Strasser, Molecular Nitrogen–Carbon Catalysts, Solid Metal Organic Framework Catalysts, and Solid Metal/Nitrogen-Doped Carbon (MNC) Catalysts for the Electrochemical $CO_2$ Reduction, *Adv. Energy Mater.*, 2018, **8**, 1703614.

6 Y. H. Pei, H. Zhong and F. M. Jin, A brief review of electrocatalytic reduction of $CO_2$-Materials, reaction conditions, and devices, *Energy Sci. Eng.*, 2021, **9**, 1012–1032.

7 B. Chang, H. Pang, F. Raziq, S. Wang, K.-W. Huang, J. Ye and H. Zhang, Electrochemical reduction of carbon dioxide to multicarbon ($C_{2+}$) products: challenges and perspectives, *Energy Environ. Sci.*, 2023, **16**, 4714–4758.

8 J. Masa, C. Andronescu and W. Schuhmann, Electrocatalysis as the Nexus for Sustainable Renewable Energy: The Gordian Knot of Activity, Stability, and Selectivity, *Angew. Chem., Int. Ed.*, 2020, **59**, 15298–15312.

9 I. M. Ul Hasan, L. W. Peng, J. F. Mao, R. N. He, Y. X. Wang, J. Fu, N. N. Xu and J. L. Qiao, Carbon-based metal-free catalysts for electrochemical $CO_2$ reduction: activity, selectivity, and stability, *Carbon Energy*, 2021, **3**, 24–49.

10 W. Lai, Y. Qiao, J. Zhang, Z. Lin and H. Huang, Design strategies for markedly enhancing energy efficiency in the electrocatalytic $CO_2$ reduction reaction, *Energy Environ. Sci.*, 2022, **15**, 3603–3629.

11 R. Purbia, S. Y. Choi, C. H. Woo, J. Jeon, C. Lim, D. K. Lee, J. Y. Choi, H.-S. Oh and J. M. Baik, Highly selective and low-overpotential electrocatalytic $CO_2$ reduction to ethanol by Cu-single atoms decorated N-doped carbon dots, *Appl. Catal., B*, 2024, **345**, 123694.

12 M. Serafini, F. Mariani, A. Fasolini, E. Scavetta, F. Basile and D. Tonelli, Nanostructured Copper-Based Electrodes Electrochemically Synthesized on a Carbonaceous Gas Diffusion Membrane with Catalytic Activity for the Electroreduction of $CO_2$, *ACS Appl. Mater. Interfaces*, 2021, **13**, 57451–57461.

13 Q. G. Zhu, X. F. Sun, D. X. Yang, J. Ma, X. C. Kang, L. R. Zheng, J. Zhang, Z. H. Wu and B. X. Han, Carbon dioxide electroreduction to $C_2$ products over copper-cuprous oxide derived from electrosynthesized copper complex, *Nat. Commun.*, 2019, **10**, 3851.

14 Y. Lum and J. W. Ager, Stability of Residual Oxides in Oxide-Derived Copper Catalysts for Electrochemical $CO_2$ Reduction Investigated with 18O Labeling, *Angew. Chem., Int. Ed.*, 2018, **57**, 551–554.

15 C. Genovese, C. Ampelli, S. Perathoner and G. Centi, Mechanism of C–C bond formation in the electrocatalytic reduction of $CO_2$ to acetic acid. A challenging reaction to use renewable energy with chemistry, *Green Chem.*, 2017, **19**, 2406–2415.

16 H. X. Wang, Y. B. Chen, X. L. Hou, C. Y. Ma and T. W. Tan, Nitrogen-doped graphenes as efficient electrocatalysts for the selective reduction of carbon dioxide to formate in aqueous solution, *Green Chem.*, 2016, **18**, 3250–3256.

17 M.-Y. Lee, K. T. Park, W. Lee, H. Lim, Y. Kwon and S. Kang, Current achievements and the future direction of electrochemical $CO_2$ reduction: a short review, *Crit. Rev. Environ. Sci. Technol.*, 2020, **50**, 769–815.

18 Y. Liu, S. Chen, X. Quan and H. Yu, Efficient Electrochemical Reduction of Carbon Dioxide to Acetate on Nitrogen-Doped Nanodiamond, *J. Am. Chem. Soc.*, 2015, **137**, 11631–11636.

19 X. F. Qiu, J. R. Huang, C. Yu, Z. H. Zhao, H. L. Zhu, Z. F. Ke, P. Q. Liao, X. M. Chen and A. Stable, and Conductive Covalent Organic Framework with Isolated Active Sites for Highly Selective Electroreduction of Carbon Dioxide to Acetate, *Angew. Chem., Int. Ed.*, 2022, **61**, e202206470.

20 B. Domingo-Tafalla, E. Martínez-Ferrero, F. Franco and E. Palomares-Gil, Applications of Carbon Dots for the Photocatalytic and Electrocatalytic Reduction of $CO_2$, *Molecules*, 2022, **27**, 1081.

21 A. R. Nallayagari, E. Sgreccia, M. L. Di Vona, L. Pasquini, F. Vacandio and P. Knauth, Nanostructured, Metal-Free Electrodes for the Oxygen Reduction Reaction Containing Nitrogen-Doped Carbon Quantum Dots and a Hydroxide Ion-Conducting Ionomer, *Molecules*, 2022, **27**, 1832.

22 A. R. Nallayagari, E. Sgreccia, L. Pasquini, F. Vacandio, S. Kaciulis, M. L. Di Vona and P. Knauth, Catalytic electrodes for the oxygen reduction reaction based on co-doped (B–N, Si–N, S–N) carbon quantum dots and anion exchange ionomer, *Electrochim. Acta*, 2022, **427**, 140861.

23 S. Syahputra, E. Sgreccia, A. R. Nallayagari, F. Vacandio, S. Kaciulis, M. L. Di Vona and P. Knauth, Influence of Nitrogen Position on the Electrocatalytic Performance of B,N-Codoped Carbon Quantum Dots for the Oxygen Reduction Reaction, *J. Electrochem. Soc.*, 2024, **171**, 8.

24 A. R. Nallayagari, E. Sgreccia, R. Pizzoferrato, M. Cabibbo, S. Kaciulis, E. Bolli, L. Pasquini, P. Knauth and M. L. Di Vona, Tuneable properties of carbon quantum dots by different synthetic methods, *J. Nanostruct. Chem.*, 2022, **12**, 565–580.

25 A. R. Nallayagari, E. Sgreccia, L. Pasquini, M. Sette, P. Knauth and M. L. D. Vona, Impact of Anion Exchange Ionomers on the Electrocatalytic Performance for the Oxygen Reduction Reaction of B-N Co-doped Carbon Quantum Dots on Activated Carbon, *ACS Appl. Mater. Interfaces*, 2022, **14**, 46537–46547.

26 P. Knauth, L. Pasquini, R. Narducci, E. Sgreccia, R. A. Becerra-Arciniegas and M. L. Di Vona, Effective ion mobility in anion exchange ionomers: relations with hydration, porosity, tortuosity, and percolation, *J. Membr. Sci.*, 2021, **617**, 118622.

27 A. E. Danks, S. R. Hall and Z. Schnepp, The evolution of 'sol–gel'chemistry as a technique for materials synthesis, *Mater. Horiz.*, 2016, **3**, 91–112.

28 A. Rigo, A. Corazza, M. L. Di Paolo, M. Rossetto, R. Ugolini and M. Scarpa, Interaction of copper with cysteine: stability of cuprous complexes and catalytic role of cupric ions in anaerobic thiol oxidation, *J. Inorg. Biochem.*, 2004, **98**, 1495–1501.

29 L. M. Salas, M. R. Salazar and B. Escobar, Doped biochar from an invasive plant "Eichhornia crassipes" for the oxygen reduction reaction, *Int. J. Hydrogen Energy*, 2022, **47**, 30140–30146.

30 N. Fechler, T.-P. Fellinger and M. Antonietti, One-pot synthesis of nitrogen–sulfur-*co*-doped carbons with tunable composition using a simple isothiocyanate ionic liquid, *J. Mater. Chem. A*, 2013, **1**, 14097–14102.

31 P. Lazar, R. Mach and M. Otyepka, Spectroscopic Fingerprints of Graphitic, Pyrrolic, Pyridinic, and Chemisorbed Nitrogen in N-Doped Graphene, *J. Phys. Chem. C*, 2019, **123**, 10695–10702.

32 A. Merlen, J. G. Buijnsters and C. Pardanaud, A Guide to and Review of the Use of Multiwavelength Raman Spectroscopy for Characterizing Defective Aromatic Carbon Solids: from Graphene to Amorphous Carbons, *Coatings*, 2017, **7**, 153.

33 P. Puech, M. Kandara, G. Paredes, L. Moulin, E. Weiss-Hortala, A. Kundu, N. Ratel-Ramond, J.-M. Plewa, R. Pellenq and M. Monthioux, Analyzing the Raman Spectra of Graphenic Carbon Materials from Kerogens to Nanotubes: What Type of Information Can Be Extracted from Defect Bands?, *C*, 2019, **5**, 69.

34 J. Wei, J. J. Sun, Y. C. Hou, Z. S. He, H. Li, S. H. Ren and W. Z. Wu, Characterization of fused aromatic multirings in lignin via synchronous fluorescence spectroscopy and catalytic hydro-depolymerization, *Microchem. J.*, 2024, **205**, 111412.

35 J. F. De Brito, C. Genovese, F. Tavella, C. Ampelli, M. V. Boldrin Zanoni, G. Centi and S. Perathoner, $CO_2$ Reduction of Hybrid $Cu_2O$–Cu/Gas Diffusion Layer Electrodes and their Integration in a Cu-based Photoelectrocatalytic Cell, *ChemSusChem*, 2019, **12**, 4274–4284.

36 S. Dongare, N. Singh and H. Bhunia, Electrocatalytic reduction of $CO_2$ to useful chemicals on copper nanoparticles, *Appl. Surf. Sci.*, 2021, **537**, 148020.

37 S. Fu, B. Tang, Z. Wang, G. An, M. Zhang, K. Wang, W. Liu, H. Guo, B. Zhang and L. Wang, Hydrophobic carbon quantum dots with Lewis-Basic nitrogen sites for electrocatalyst $CO_2$ reduction to $CH_4$, *Chem. Eng. J.*, 2024, **500**, 157207.

38 B. Hedau, S.-J. Park, B.-C. Kang and T.-J. Ha, Bifunctional carbon quantum dot-embedded metal-organic framework nanohybrid as a highly efficient electrocatalyst for water splitting and $CO_2$ reduction, *Carbon*, 2024, **216**, 118527.

39 H. Guo, J. Raj, Z. Wang, T. Zhang, K. Wang, L. Lin, W. Hou, J. Zhang, M. Wu, J. Wu and L. Wang, Synergistic Effects of Amine Functional Groups and Enriched-Atomic-Iron Sites in Carbon Dots for Industrial-Current–Density $CO_2$ Electroreduction, *Small*, 2024, **20**, 2311132.

40 L. Deng, H. Yuan, X. Qian, Q. Lu, L. Wang, H. Hu and Y. Chen, Municipal sludge-derived carbon dots-decorated, N-doped hierarchical biocarbon for the electrochemical reduction of carbon dioxide, *Resour., Conserv. Recycl.*, 2022, **177**, 105980.

41 D. Ríos-Ruiz, P. Arévalo-Cid, J. Cebollada, V. Celorrio and M. V. Martínez-Huerta, Tailoring of single copper atoms anchored on N,P co-doped carbon for electrochemical $CO_2$ reduction, *Catal. Today*, 2025, **454**, 115284.

42 M. H. Suliman, Z. H. Yamani and M. Usman, Electrochemical Reduction of $CO_2$ to C1 and C2 Liquid Products on Copper-Decorated Nitrogen-Doped Carbon Nanosheets, *Nanomaterials*, 2023, **13**, 47.

43 C. Wang, G. Zhang, R. Luo, Y. Wang, X. Ma, M. Zhang, X. Chang, Z. J. Zhao, T. Wang and J. Gong, Selective CO(2)

reduction to acetate via controlled sp(2)/sp(3) carbon hybridization, *Nat. Commun.*, 2025, **16**, 10506.

44 R. Bhaskaran, B. G. Abraham and R. Chetty, Recent advances in electrocatalysts, mechanism, and cell architecture for direct formic acid fuel cells, *WIREs Energy Environ.*, 2022, **11**, e419.

45 S. Zhang, P. Kang, S. Ubnoske, M. K. Brennaman, N. Song, R. L. House, J. T. Glass and T. J. Meyer, Polyethylenimine-Enhanced Electrocatalytic Reduction of $CO_2$ to Formate at Nitrogen-Doped Carbon Nanomaterials, *J. Am. Chem. Soc.*, 2014, **136**, 7845–7848.

46 M. Orlic, C. Hochenauer, R. Nagpal and V. Subotic, Electrochemical reduction of $CO_2$: a roadmap to formic and acetic acid synthesis for efficient hydrogen storage, *Energy Convers. Manage.*, 2024, **314**, 118601.

47 H. Y. Wang, J. Xue, C. X. Liu, Z. Y. Chen, C. B. Li, X. Li, T. T. Zheng, Q. Jiang and C. Xia, $CO_2$ electrolysis toward acetate: a review, *Curr. Opin. Electrochem.*, 2023, **39**, 101253.

48 H. Xiao, W. A. Goddard, T. Cheng and Y. Liu, Cu metal embedded in oxidized matrix catalyst to promote $CO_2$ activation and CO dimerization for electrochemical reduction of $CO_2$, *Proc. Natl. Acad. Sci. U. S. A.*, 2017, **114**, 6685–6688.

49 T. Zhang, J. He and X. Xiang, Precise Construction of Cu-Based Catalysts using Surface Molecular Modifiers for Electroreduction of $CO_2$ to Multi-Carbon Products, *ChemCatChem*, 2023, **15**, e202301119.

50 Y. B. Melnichenko, N. V. Lavrik, E. Popov, J. Bahadur, L. He, I. Kravchenko, G. Smith, V. Pipich and N. K. Szekely, Cavitation on deterministically nanostructured surfaces in contact with an aqueous phase: a small-angle neutron scattering study, *Langmuir*, 2014, **30**, 9985–9990.

51 A. C. Pérez-Sequera, M. A. Díaz-Pérez and J. C. Serrano-Ruiz, Recent Advances in the Electroreduction of $CO_2$ over Heteroatom-Doped Carbon Materials, *Catalysts*, 2020, **10**, 1179.

52 R. D. Pike, Structure and Bonding in Copper(I)Carbonyl and Cyanide Complexes, *Organometallics*, 2012, **31**, 7647–7660.

53 R. M. Arán-Ais, F. Scholten, S. Kunze, R. Rizo and B. Roldan Cuenya, The role of in situ generated morphological motifs and Cu(I) species in $C_{2+}$ product selectivity during $CO_2$ pulsed electroreduction, *Nat. Energy*, 2020, **5**, 317–325.

54 H. H. Heenen, H. Shin, G. Kastlunger, S. Overa, J. A. Gauthier, F. Jiao and K. Chan, The mechanism for acetate formation in electrochemical CO(2) reduction on Cu: selectivity with potential, pH, and nanostructuring, *Energy Environ. Sci.*, 2022, **15**, 3978–3990.

55 C. Zhang, T. Liu and B. Lu, Electrocatalytic $CO_2$ Reduction over Pyridinic Nitrogen-Doped Carbon as a Metal-Free Catalyst, *Langmuir*, 2025, **41**, 29400–29411.

56 C. Dong, L. Cui, Y. Kong, C. Chen, H. Liu, Y. Zhang, W. Zhu and R. He, Elemental Doping Induced Sulfur Vacancies Enable Efficient Electrochemical Reduction of $CO_2$ over CdS Nanorods, *J. Phys. Chem. C*, 2022, **126**, 102–109.